



ELSEVIER

Contents lists available at ScienceDirect

## Journal of Magnetism and Magnetic Materials

journal homepage: [www.elsevier.com/locate/jmmm](http://www.elsevier.com/locate/jmmm)

## Differential permeability behaviour of P9 and T22 power station Steels

N. Karimian<sup>a,\*</sup>, J.W. Wilson<sup>a</sup>, A.J. Peyton<sup>a</sup>, W. Yin<sup>a</sup>, J. Liu<sup>b</sup>, C.L. Davis<sup>b</sup><sup>a</sup> School of Electrical and Electronic Engineering, University of Manchester, M60 1QD, UK<sup>b</sup> School of Metallurgy and Materials, University of Birmingham, Edgbaston, Birmingham B15 2TT, UK

## ARTICLE INFO

## Article history:

Received 24 July 2013

Received in revised form

25 September 2013

Available online 16 October 2013

## Keywords:

Electromagnetic property

Power station steel

Electromagnetic sensor

Hysteresis curve

Differential permeability

## ABSTRACT

Analysis of the electromagnetic (EM) properties of power station steels, measured using a non-contact magnetic sensor, is of significance as such properties are indicative of the microstructure of the material and can be potentially exploited for non-destructive testing. In this paper, we present EM measurements of cylindrical power station steel samples (P9 and T22 grades) with different microstructures: normalised and tempered (representative of the initial condition), as normalised and after service exposure. In order to obtain the magnetic properties the  $B-H$  curves of these samples were measured. Cylindrical air-cored and printed circuit board (PCB) coil integrated sensors were used to measure the incremental permeability. Analytical and numerical methods (Finite Elements Methods) were employed to calculate the sensor response of these samples. The electromagnetic properties of the different steels were inferred by fitting the finite element models to the measured results. In addition, sensitivity and error analysis were carried out to evaluate the accuracy of the method.

© 2013 Elsevier B.V. All rights reserved.

## 1. Introduction

Measurement of the electromagnetic (EM) properties of materials can be very important; as such properties give an indication of the materials' microstructure (and hence performance) and condition-related parameters. For instance, the permeability and conductivity of porous Cu and Fe foams, manufactured by the lost carbonate sintering process, have proven to be related to their porosity [1]. In steels, ferrite fraction variations [2–5] creep damage and precipitation [6,7] cause changes to the EM properties. Factors such as mechanical compression [8] mechanical stress [9,10] residual stress [11] aging, temperature and case hardening [12–16] also affect the steels' EM properties. Such EM properties can be obtained through inspection of the material using purpose built EM sensors.

Power generation steel components such as boiler tubes and steam line pipes are exposed to high temperature and pressure during their lifetime, and therefore experience carbide coarsening and occurrence of creep cavitation [17] possibly leading to component failure. To the authors' knowledge, no in-situ technique has yet been implemented to directly monitor the changes in microstructure of in-service power station steel components at an elevated temperature. It is worth noting that incorrect heat treatment of power station steels (i.e. P9 and T22) prior to going into service can result in a ferritic structure, which can be problematic. Coal-fuelled

power stations can currently operate at temperatures of up to 620 °C, but this may increase within the next decade to around 700 °C for future operations in order to help reduce their carbon dioxide (CO<sub>2</sub>) emissions by up to 25%, and also provide greater efficiency. For instance, the supercritical power stations could produce output efficiencies of 45% to 50%, compared to subcritical power stations with efficiencies of 30% to 35%. The increase in operating temperatures may lead to a requirement for more frequent and detailed inspections. Also new steels may need to be employed as well as better non-destructive evaluation procedures to monitor the degradation in microstructure with time, to ensure that end-of-life conditions are not reached.

Currently the condition of power station components are monitored during costly shut down periods, when insulating lagging layers are removed and replicas from the component surface are made. These replicas are examined to determine the microstructural state (degree of degradation, e.g. through carbide population changes) and whether creep cavitation has initiated. Components are removed from service and replaced when end of predicted service life is reached or significant cavitation is detected; and since the component condition can only be checked during a scheduled shut down period, sections are often replaced prematurely. However if failure of a component occurs the economic impact is severe, i.e. an unplanned shutdown is estimated to cost approximately \$2 M per day per power station, and there is potentially significant risk to life and the environment.

Magnetic induction techniques have been used extensively in measuring the EM properties of materials at relatively low frequencies (i.e. < 10 MHz). In doing so, various sensor configurations have

\* Corresponding author. Tel.: +44 1613068902.

E-mail address: [Noushin.Karimian@Manchester.ac.uk](mailto:Noushin.Karimian@Manchester.ac.uk) (N. Karimian).

been used, for example, cylindrical air-cored sensors [18,19] H-shaped ferrite-core coils and printed circuit board (PCB) based planar coils [20]. Sensor arrays have also been used in imaging and fault detection. In particular, a considerable amount of research has been carried out on a relatively new technique called Magnetic Inductance Tomography (MIT) [21–27]. It is also important to note that, many authors have developed various computation algorithms, ranging from analytical to numerical ones, in order to predict and evaluate the performance of the sensor and sensor array [28–32].

Undoubtedly, the ability to monitor microstructural changes in steel components through their EM property variation has great potential and may become very useful in the future. In this paper, cylindrical air-cored and PCB-coil integrated sensors were designed to measure the EM properties of 50 mm long cylindrical power generation steel (P9 and T22) samples removed from service or heat treated to give different microstructures. Naturally, other sensor geometries for component investigations are also possible. The EM properties of these steel samples, which have been obtained through impedance measurements using the two sensor geometries, are then compared with each other. Analytical and numerical methods (finite elements (FE)) have been used to calculate the sensor response, through which the conductivity and permeability of the samples were inferred. In addition, the relative incremental permeability of P9 and T22 steel samples have been obtained through the measurement of minor loop deviations from the initial magnetisation curve, the results of which are connected to the permeability values obtained from the spectroscopy of these samples. A sensitivity analysis was also carried out to evaluate the accuracy of the method [19].

## 2. Methodology

### 2.1. Physical principle

Any microstructural variation in steel may lead to changes in its EM properties, e.g. permeability and conductivity. EM sensors function on the basis of detecting and identifying variations in these quantities measured from samples. By measuring the response of such EM sensors over a range of frequencies, the permeability and conductivity of steels can then be inferred.

The effect of eddy currents on the sensor response is very weak at low frequencies, and any contribution to the inductance change is mainly from the magnetisation of the sample. Therefore the inductance measured at low frequencies is related to the sample permeability. However, the effect of eddy currents in the sample becomes stronger with increasing frequency; and therefore variations in inductance are gradually dominated by the effect of conductivity or polarisation delay of the sample. The electric and magnetic properties of the samples can be determined by complete analysis of the inductance–frequency spectra.

### 2.2. Experimental procedure

Two power generation steels, removed from service at 520 °C for approximately 11 years, were studied: P9 steel (8.40 Cr–0.97 Mo–0.12 C–0.52 Si–0.44 Mn all wt%) and T22 steel (1.90–2.60 Cr–0.87–1.13 Mo–0.05–0.15 C–0.50 Si–0.30–0.60 Mn all wt%). Samples measuring approximately 70 mm × 15 mm × 7 mm were machined from the as-received (ex-service) material and heat treated to simulate the service entry microstructure by normalising at 950 °C or 940 °C for 1 hour and then tempering at 760 °C for 1 hour or 720 °C for 1.5 hours, for the P9 and T22 steels respectively.

In addition to the tempered and ex-serviced samples, as normalised samples were also examined. Cylindrical rods of 50 mm long

and 4.95 mm in diameter for each condition were prepared for the EM sensor measurements.

The EM properties of the samples were measured using two different coaxial probes. Firstly an air-cored cylindrical sensor, consisting of two identical coils arranged with their axes aligned, one exciting and the other receiving. The coils have a length of 9.8 mm, inner diameter of 6.9 mm and outer diameter of 8.3 mm with a separation of 10.4 mm. Secondly, an air-cored PCB-coil integrated sensor, which also consists of two identical coils, arranged as PCB layers on top of each other, one exciting and the other receiving. The PCB-coil integrated sensor consists of 12 layers, 6 of which contain the coils for the receiver and the remaining 6 for the transmitter. Each of these 6 layers consists of 6 turns, making 36 turns for each transmitter and receiver. The thickness of each turn (line width), as well as the distance between each turn (separation space) is 0.2 mm. The distance between the steel and the first turn on each layer is 1 mm. The coils have a length of 1.6 mm, inner diameter of 7 mm and outer diameter of 11.4 mm with a separation of 1 mm. Measurements of trans-impedance were taken with an impedance analyser (Solartron 1260) at frequencies from 10 Hz to 1 MHz. The geometry and setup for the two sensor measurements are shown in Fig. 1.

### 2.3. Sensor analytical model and FE simulation

Assuming an infinitely long coil encircling an infinitely long cylindrical sample, an analytical solution can be established from Maxwell's Equations [17] to determine its impedance:

$$\frac{L}{L_{air}} = 1 - \eta + \frac{2\eta u_1}{\alpha u_0} \left( \frac{J_1(\alpha) + VY_1(\alpha)}{J_0(\alpha) + VY_0(\alpha)} \right) \quad (1)$$

Where  $\eta = d^2/d_c^2$  is the fill factor,  $d_c$  is the diameter of the coil and  $d$  is the diameter of the rod sample.  $J$  and  $Y$  are, respectively, Bessel functions of the first and second order,  $V$  indicates that  $Y_0$  and  $Y_1$  are Imaginary Bessel function,  $\mu_0$  is the permeability of free space, and  $L_{air}$  is the electrical impedance of the empty coil.

In the limit of low frequency, i.e. when  $f \rightarrow 0$  then:

$$\frac{L}{L_{air}} = 1 - \eta + \eta \frac{\mu}{u_0} \quad (2)$$

Suppose we use the empty coil as reference, then:

$$\frac{L - L_{air}}{L_{air}} = \eta \left( \frac{\mu}{u_0} - 1 \right) \quad (3)$$

From Eq. (3), it can be seen that the inductance difference has a linear relationship with the permeability of the steel sample. For cases where the length of the coil is finite, then the analytical solution becomes nonlinear and therefore significantly more complicated.

The above analytical solutions are only valid for simplified geometries (i.e. infinitely long samples placed coaxially in a finite or an infinitely long coil), therefore FE models which take in full account the sensor and sample interaction, were built in Maxwell 12.0 (ANSYS, Inc.) to model the actual measurement arrangement, in order to determine the relative permeability and conductivity by fitting with the experimental data (see Fig. 2).

## 3. Measurement and experimental results

### 3.1. Metallographic tests

Metallographic tests on the P9 and T22 grade samples to analyse the microstructure of the samples in the as received (ex-service) condition and after heat treatments have been carried out and presented previously [18,19,33]. However, for completeness, the

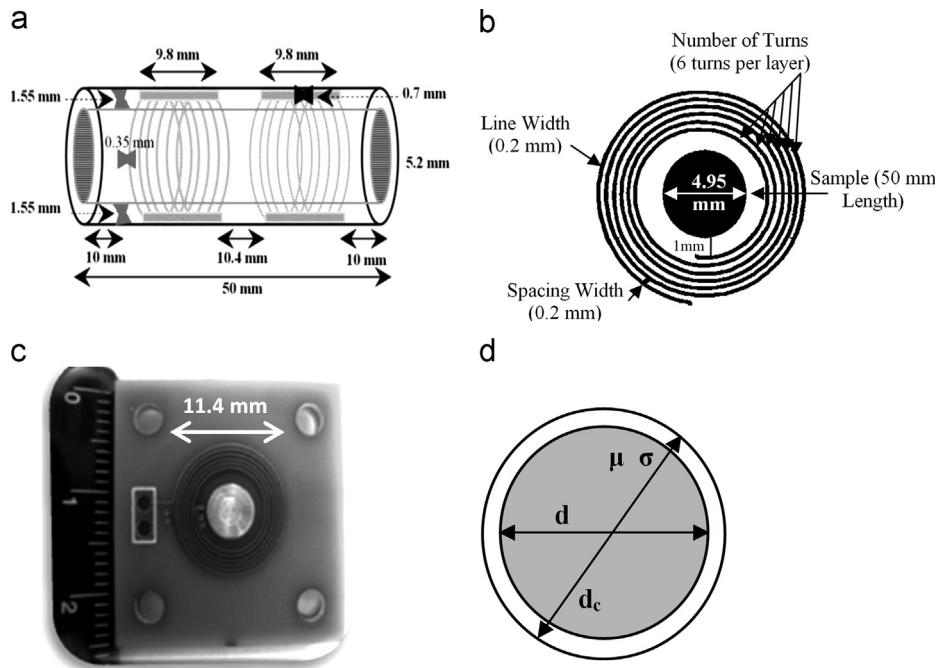


**Fig. 1.** (a) The air-cored cylindrical sensor and sample setup [19], (b) the geometry of each layer of the coil for the PCB-coil integrated sensor, (c) the fabricated PCB-coil integrated sensor with 6 layers on each receiver and transmitter and (d) the geometry of the coil and the steel sample for the example presented in Section 2.3.

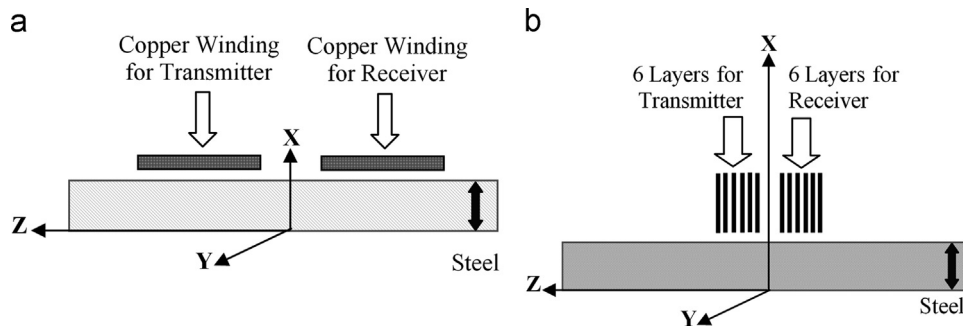


**Fig. 2.** Axis symmetrical FE model for the sample and sensors: (a) air-cored cylindrical sensor, (b) PCB-coil integrated sensor – Note Z is the axis of rotational symmetry.

microstructures of the P9 and T22 samples in the different conditions are shown in Figs. 3 and 4. As shown in Fig. 3(a), the microstructure of the as-normalised P9 consists of predominantly martensite mixed with some bainite. Subsequent tempering produces a simulated service entry microstructure, i.e. tempered martensite/bainite as shown in Fig. 3(b). After long service exposure, the microstructure showed equiaxed ferrite with large carbides distributed within ferrite grains or on grain boundaries, as shown in Fig. 3(c).

The as-normalised T22 steel shows a mixed microstructure of bainite and some proeutectoid ferrite, as shown in Fig. 4(a). No carbides are present in the ferrite, but plate-like carbides can be seen within the bainite regions. After tempering, many carbides can be observed along prior austenite grain boundaries, on ferrite boundaries or within bainite regions, as shown in Fig. 4(b). The microstructure of T22 after the service exposure consists of equiaxed ferrite and a great many carbides outlining the ferrite grain boundaries or finely dispersed within the ferrite grains, as shown in Fig. 4(c).

### 3.2. EM sensor measurements

The measured mutual inductance spectra for P9 and T22 in different conditions are shown in Fig. 5.

The real inductance graphs, shown in Fig. 5(a) and (b), have a characteristic shape, with a flat section for frequencies below approximately 500 Hz; a roll off over the intermediate frequencies and finally a flat high frequency response. The flat low frequency response is determined by the differential permeability of the sample, suggesting that the permeability is constant with frequency at least up to 500 Hz. The roll-off over the intermediate frequency response results from eddy currents circulating coaxially in the sample; here the electromagnetic skin depth is reducing with frequency and eventually becomes much smaller than the radius of the sample. At high frequencies, the skin depth effectively approaches zero and the real mutual inductance approaches a constant slightly negative value determined only by the dimensions of the coil/sample geometry; the cylindrical sensor (Fig. 5(a)) reaches this at approximately 100 kHz; however the response for the PCB sensor (Fig. 5(b)) still reduces at 1 MHz, illustrating that different coil geometries offer quite different frequency responses for the same sample.

The graphs of the imaginary component in Fig. 5(c) and (d) all show a characteristic curve with a maximum response which coincides with maximum energy transfer eddy current heating from the transmitter coil to the sample. As it can be observed from Fig. 5, the P9 and T22 steel samples with different microstructures produce different curves, indicating that the samples have different EM properties.

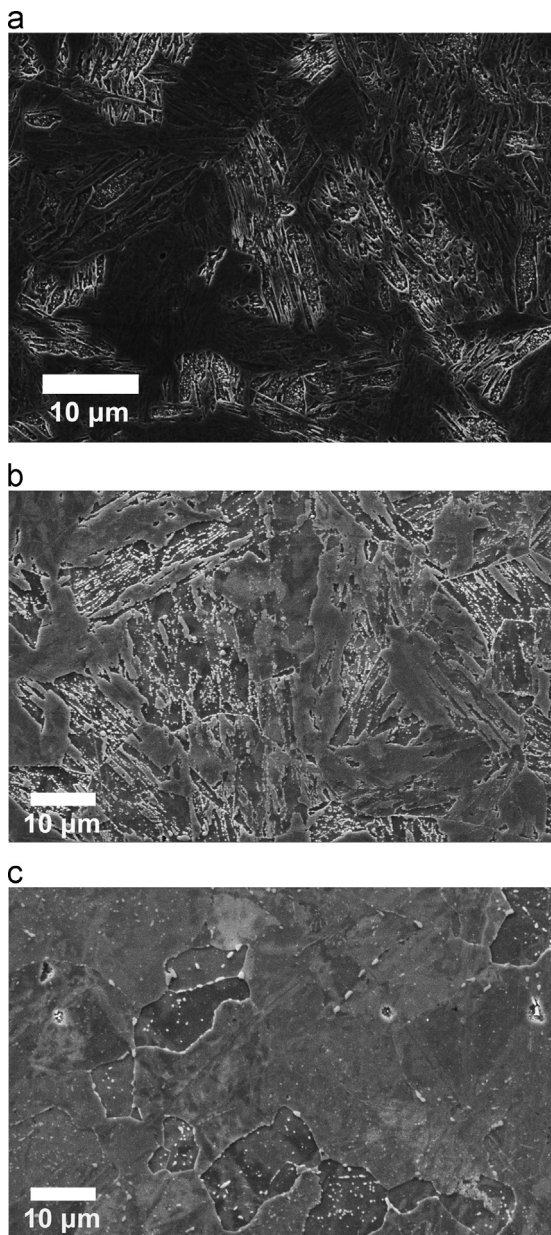


**Fig. 3.** Microstructure of the P9 samples in different conditions: (a) as normalised (b) as tempered and (c) ex-service.

### 3.3. Effect of residual magnetic field on inductance readings

In real world applications, ferromagnetic components will often be magnetised to a certain level, from previous magnetic/electromagnetic inspection, spontaneous magnetisation, etc. Thus it is essential that any technique employed for inspection is tolerant to differing levels of magnetisation. Fig. 6 shows the results of an experiment to assess the effect of residual magnetisation on the measured inductance. The samples were magnetised to different levels using the apparatus shown in Fig. 7, the residual magnetisation was measured using a Hall sensor after removal from the magnetising U-core and the samples were inspected using the technique described in Section 3.2. Fig. 6 shows the real mutual inductance for each sample at 100 Hz with respect to the residual magnetisation. It is worth noting that when magnetising the samples to produce the residual fields, applied fields of up to 10 kA/m were used; however the maximum residual magnetisation for these samples is only 2.5, 0.5 and 0.3 kA/m for the

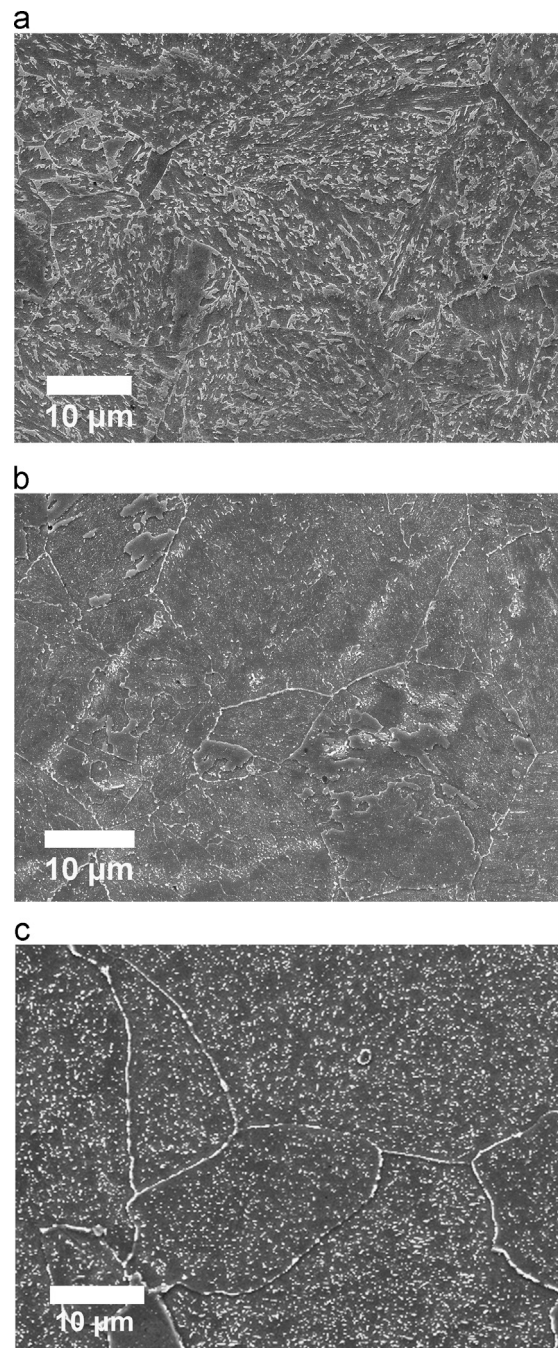


**Fig. 4.** Microstructure of the T22 samples in different conditions: (a) as normalised (b) as tempered and (c) ex-service.

normalised (magnetically harder), tempered and ex-service (magnetically softer) respectively. The maximum values of residual magnetisation for these differently heat-treated samples are dependent on microstructure; different heat treatments change the crystal lattice of the material, which in turn affects the magnetic domain structure, which determines the maximum level of magnetisation. It is clear from Fig. 6 that an increase in applied field causes an increase in residual field and a corresponding increase in inductance. It can also be seen from the plot, that although the residual field does have some impact on the measured inductance, the variation in inductance is relatively small for these samples. However, if components cannot be effectively demagnetised this variation should be taken into account as a potential source of error.

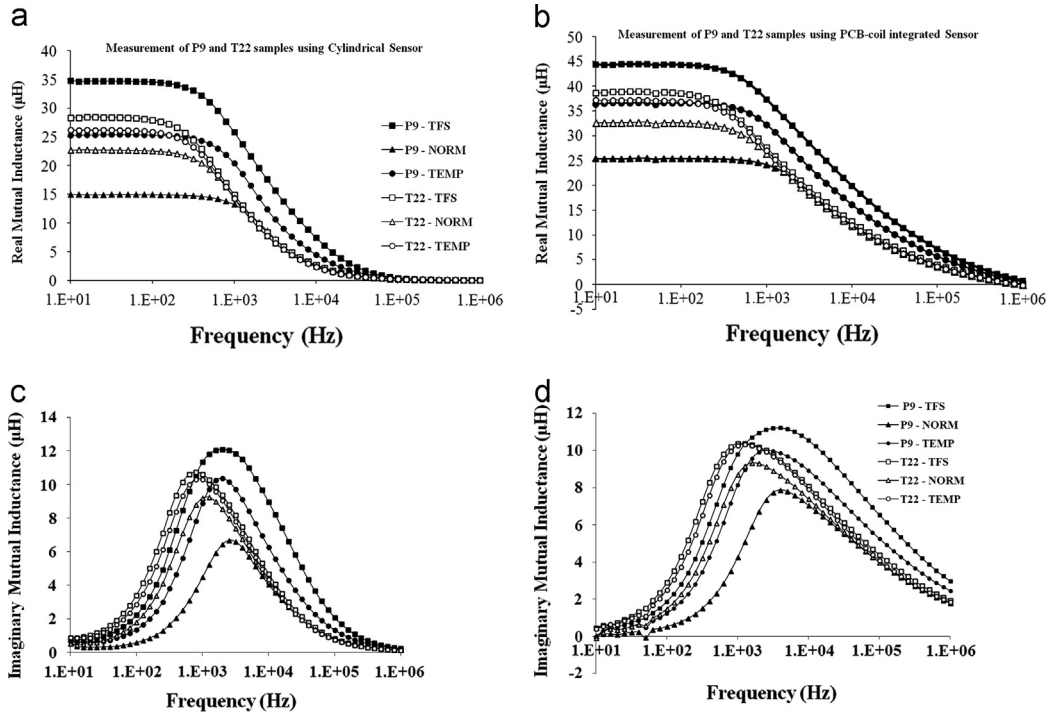


Fig. 5. The inductance spectra for P9 and T22 samples with different conditions (a) the real inductance spectra for cylindrical air-cored sensor, (b) real inductance spectra for PCB-coil integrated sensor, (c) the imaginary inductance spectra for cylindrical air-cored sensor and (d) imaginary inductance spectra for PCB-coil integrated sensor – (TFS: Taken from Service, NORM: Normalised, and TEMP: Normalised and Tempered).

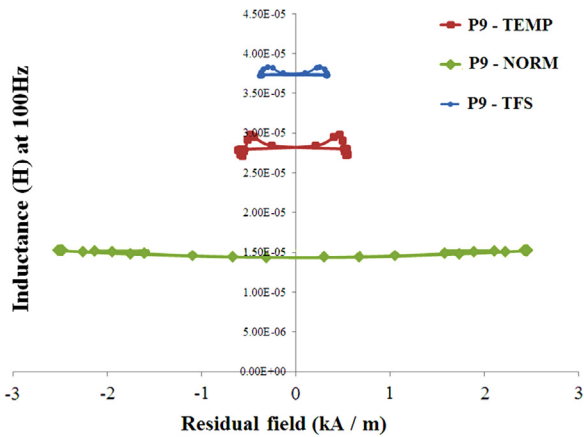


Fig. 6. Investigating the effect of residual magnetic field on real mutual inductance readings.

By comparing Figs. 6 to 10b, the change in inductance for the residual field and the change in permeability at different points on the major loop can be observed. It is notable that only half a cycle is shown for permeability; whereas a full cycle is shown for inductance (Fig. 6), thus the inductance plot has two peaks. The effect shown in the two figures are comparable. In Fig. 10b permeability peaks at approximately  $H_C$  (the point at which  $B=0$ ) and domain walls have the greatest degree of freedom to move; whereas in Fig. 6, the inductance peaks at a point where the residual magnetisation results in a domain structure which is preferable for the field applied for the inductance measurements. As the field applied to magnetise the samples is in the same direction as the field applied to measure inductance, magnetisation of the samples results in domains aligning with the magnetic easy axes closest to the field applied for inductance measurement.

### 3.4. B–H measurements

Another aspect of obtaining the magnetic properties of a sample is to measure its magnetic hysteresis [34]. So far several mathematical models have been proposed in order to study the hysteresis of magnetic materials. In particular, the classical scalar Preisach model (CSPM) has been successfully employed [35–38]. The  $B-H$  curves for the three P9 and T22 steel samples with different microstructures have been measured. The reason for such measurement is to obtain the relative incremental permeability of these power station steels through their magnetic hysteresis, results of which are connected to the permeability values obtained from the spectroscopy of these samples.

In order to obtain the hysteresis loop (major loop), a sinusoidal excitation of 0.5 Hz was used and 9 excitation cycles were recorded and averaged. A sinusoidal excitation of 10 Hz was used to generate the minor loops, with two types of minor loop being recorded; (1) deviations from the main  $B-H$  loop. In this case, the sample was taken through several major loop cycles before the applied field is held constant at a pre-determined H value and

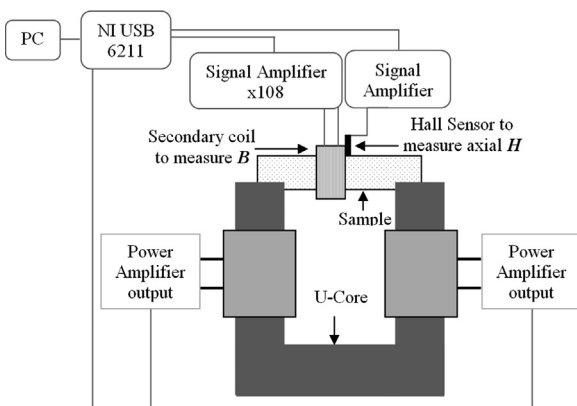


Fig. 7. Setup for the  $B-H$  measurements.

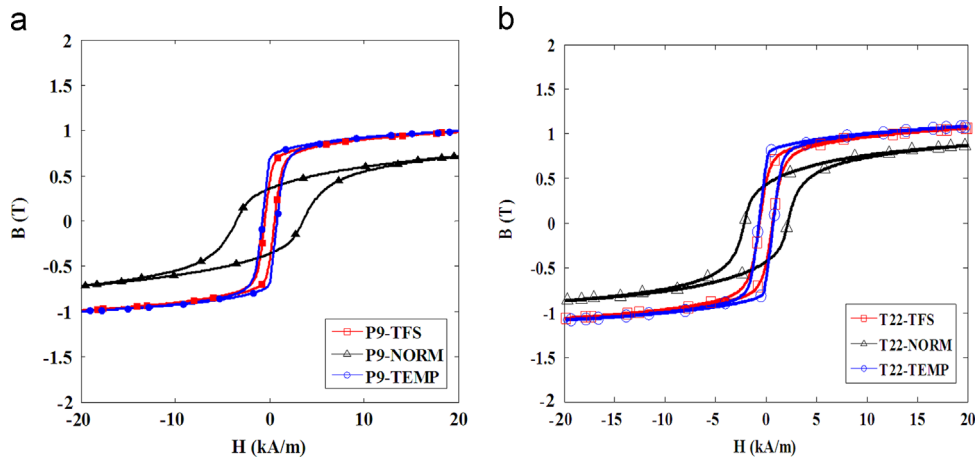


Fig. 8.  $B$ - $H$  measurements for (a) P9 and (b) T22 samples with different conditions (TEMP: Tempered, NORM: Normalised, and TFS: Taken From Service).

Table 1

Summary of the relative permeability, conductivity, coercivity ( $H_C$ ) values for the different P9 and T22 steel samples.

Samples and conditions		$\mu_R$ obtained from cylindrical sensor	$\mu_R$ obtained from PCB sensor	Conductivity (MS/m)	$\mu_i$ obtained from $B$ - $H$ curves	Coercivity (A/m)
<b>P9</b>						
NORM	Normalised	28.7	29.5	1.69	22.0	3.514
TEMP	Normalised and tempered	52	62	1.82	55.2	0.778
TFS	Taken from service	83	109	1.83	90.9	0.512
<b>T22</b>						
NORM	Normalised	45.1	48	2.99	36.9	2.154
TEMP	Normalised and tempered	53.9	65.5	3.53	48.5	0.718
TFS	Taken from service	60.4	72.5	3.87	57.4	0.644

several minor loop cycles were recorded; and (2) deviations from the initial magnetisation curve. The sample was demagnetised by the application of 10 Hz sinusoidal excitation, reducing in amplitude over a period of 10 s. The applied field was then increased to a pre-determined  $H$  value and several minor loop cycles recorded. For both types of minor loop, up to 90 cycles are acquired and averaged, to reduce noise, especially for very low applied field values. The setup for such measurement is presented in Fig. 7.

The measured  $B$ - $H$  curves for the P9 and T22 samples are illustrated in Fig. 8. As it can be seen from Fig. 8, different power station steel samples produce different  $B$ - $H$  curves. The  $B$ - $H$  curves demonstrate the micro-magnetic properties of steels including coercivity, remanence, saturation magnetisation, etc. These properties, and the relative permeability, are affected by different microstructural features. Therefore,  $B$ - $H$  measurement and EM sensor measurement can be seen as complementary techniques.

As shown in Fig. 8, the  $B$ - $H$  loops for both sets of samples (P9 and T22) follow the same trend; the ex-service sample results in the lowest coercivity ( $H_C$ ), with a small increase in  $H_C$  for the tempered samples and a large increase in  $H_C$  for the normalised samples (Table 1). The coercivity values reflect the magnetic hardness of the samples, which in turn is indicative of material hardness. As the P9 normalised sample is predominantly martensitic with a Vickers hardness value of HV401, it exhibits the greatest  $H_C$  value. As bainite typically has a lower hardness than as-quenched martensite, but higher hardness than ferrite, the bainite/pro-eutectoid ferrite microstructure of the T22 normalised sample (HV316) shows a reduction in  $H_C$  in comparison to the P9 normalised sample. The difference between the ex-service and

tempered samples is less pronounced, with a decrease in hardness after the in-service exposure being reflected by a small decrease in  $H_C$  for both sample sets; with HV212 and HV203 for P9 and T22 TEMP and also HV158 and HV129 for P9 and T22 TFS respectively.

Fig. 9 shows the evolution of the minor loop as deviations from the initial magnetisation curve. The origin of the first minor loop corresponds to the demagnetised state, where  $B$  and  $H$  are equal to zero. As the initial magnetisation curve approaches saturation, domain walls are swept away by field pressure. The dominant magnetisation mechanism can be described as the progressive alignment of the field against anisotropy, as the domains rotate from their magnetic easy axes towards the direction of the applied field [39]. Consequently, only the reversible components remain, resulting in a closed loop, with a smaller variation in  $B$  for a given applied field, as shown in Fig. 9 (bottom right).

As it is illustrated in Fig. 9, the incremental permeability ( $\mu_\Delta$ ) can be obtained from the minor loops. Such a quantity can be calculated as the ratio of the variation in flux density ( $\Delta B$ ) and the corresponding change in the applied field ( $\Delta H$ ), scaled with respect to the permeability of free space ( $\mu_0$ ); presented in

$$\mu_\Delta = \frac{1}{\mu_0} \times \frac{\Delta B}{\Delta H} \quad (4)$$

The resultant incremental permeability curves for the P9 steel samples with different microstructures, obtained from the minor loop deviations from the initial magnetisation curve, are shown in Fig. 10a. As it is clear from this figure, the maximum permeability values for the initial magnetisation curves correspond to the initial permeability ( $\mu_i$ ) reading; the point at which domains have the greatest degree of freedom to overcome pinning sites, resulting in

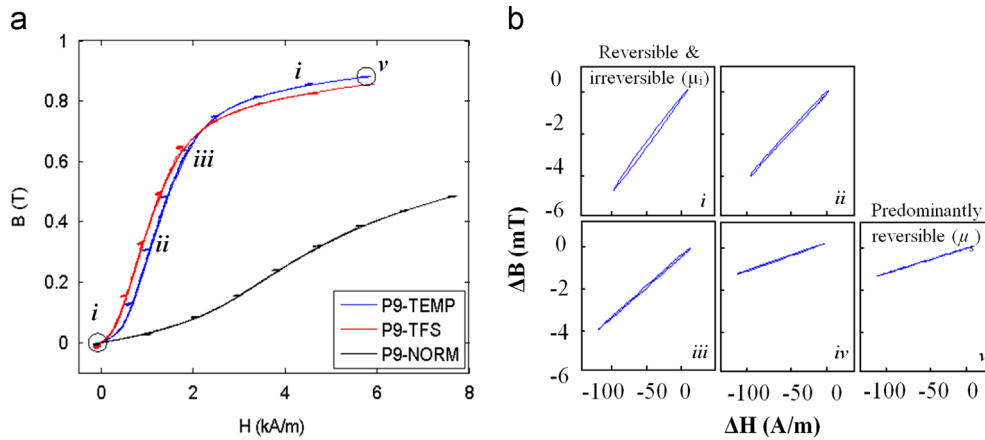


Fig. 9. (a) Initial magnetisation curves and (b) minor loop deviations for P9 Tempered sample –  $B$  and  $H$  offsets removed from minor loops for comparison.

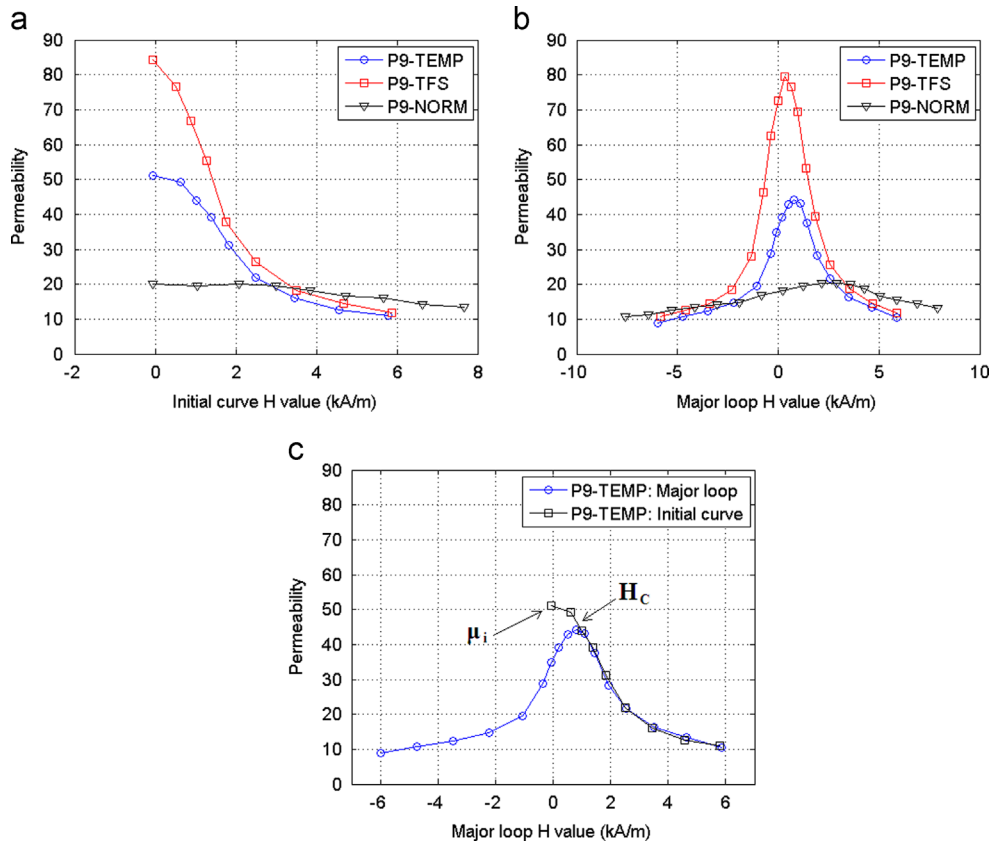


Fig. 10. (a) Incremental permeability curves for initial magnetisation of P9 samples, (b) incremental permeability curves for major  $B$ – $H$  loop, and (c) incremental permeability curves for initial magnetisation and major  $B$ – $H$  loop for sample P9-TEMP.

the greatest change in  $B$  for a given applied field. A sharp decrease of incremental permeability value with increase in applied field, along with near convergence in  $\mu_{\Delta}$  values for the three samples can also be observed. The convergence is the point at which saturation is approached and contributions from domain wall pinning sites are reduced, giving way to reversible domain rotation effects.

The incremental permeability curves for minor loop deviations from the major  $B$ – $H$  loop are shown in Fig. 10b; it is important to note that only the incremental permeability curves corresponding to one half of the major  $B$ – $H$  loop (increasing  $B$ ) are shown for clarity. As it is apparent from this figure, the maximum incremental permeability value (the peak of the curve) corresponds to a positive  $H$  value; in the region of coercive field where  $B=0$  and the domain walls have the greatest degree of freedom to move.

Fig. 10c shows the superimposed curves for the P9 tempered sample from Fig. 10a and b. It is clear that although the incremental permeability curves for initial magnetisation and major  $B$ – $H$  loop have different values at  $H=0$ , they converge at the coercive field ( $H_c$ ). From both Figs. 9 and 10c, it is apparent that the random domain distribution of the demagnetised sample, where  $H=B=0$ , corresponding to the  $\mu_i$  reading, results in a greater variation in  $B$  for a given  $H$  field than the systematic re-organisation of domains at  $H_c$ .

### 3.5. Permeability and conductivity evaluation

Finite element models were setup to simulate the sensor response. The simulated results are compared to the measured results to fit the

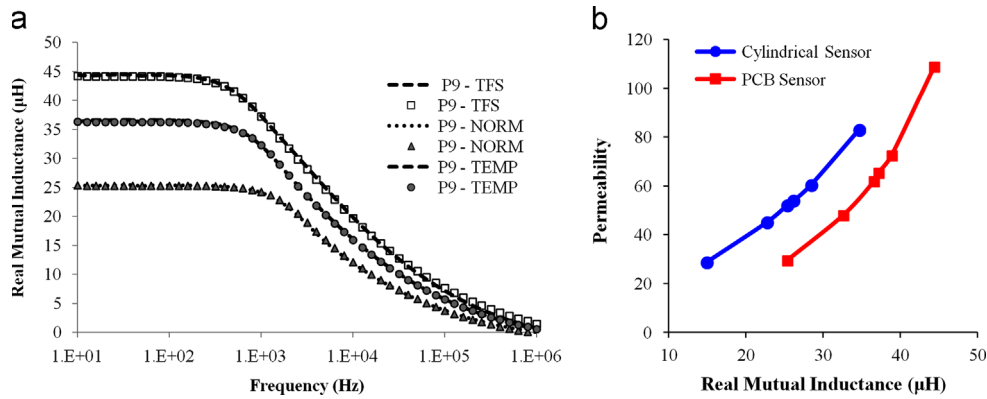


**Fig. 11.** (a) Fitting for P9 samples; comparison of the simulated results with the measured results taken using the PCB sensor (dotted lines for measurements and markers for simulation) and (b) calibration curves – relative permeability versus real mutual inductance at 20 Hz for both the cylindrical air-cored and PCB sensors.

conductivity and permeability in a least squared sense for both the cylindrical and PCB-coil integrated sensors. The comparison of the simulated results with the measured results for the cylindrical sensor has been covered in [13]. Fig. 11(a) shows the comparison of the simulated with the measured results for the P9 samples using the PCB-coil integrated sensor. It is evident from Fig. 11(a), that the measurement and simulation results are in good agreement. Permeability and conductivity values for the P9 and T22 samples can therefore be inferred, a list of which is provided in Table 1. Fig. 11 (b) shows the calibration curves for the real mutual inductance values measured at 20 Hz versus the relative permeability for both the cylindrical air-cored and PCB sensors. This graph shows that the geometry of the two sensors has an effect on the absolute values, but the relationship between permeability and real inductance is similar.

Table 1 presents the permeability values for the power station steels (P9 and T22) for both impedance analyser measurement (using the cylindrical air-cored and the PCB-coil integrated sensors) and also their corresponding coercivity values obtained from the magnetic hysteresis loop measurements. It is interesting to see how the permeability values for P9 and T22 normalised, tempered and ex-serviced samples increase from small to large values respectively.

By comparing the metallographic observation presented in Figs. 3 and 4 and the magnetic permeability values presented in Table 1, it can be seen that the ex-service P9 sample, with equiaxed ferrite with large carbides distributed within ferrite grains or on grain boundaries, has a higher magnetic permeability value. On the other hand, the samples with large amount of martensite/bainite produce a lower magnetic permeability. Therefore, there is a correlation between the metallographic observations and the obtained magnetic properties for these materials, this is discussed in more detail elsewhere [27].

It is also evident that when a series of samples all have basically similar metallurgical microstructure, i.e. the tempered P9 and T22 samples, which are all forms of tempered martensite/bainite, then the variation in permeability is very small. Thus, the permeability values for the P9 and T22 tempered samples (P9-TEMP and T22-TEMP) fall into a narrow range of 52–53.9 and 62–65.5 for the cylindrical and PCB-coil integrated sensor respectively. However, when there is a significant microstructural difference, there is a big change in permeability. As a result, the samples with un-tempered martensitic microstructures (P9-NORM and T22-NORM) have permeability of 28.7 and 45.1 for the cylindrical sensor; and 29.5 and 48 for the PCB-coil integrated sensor. On the other hand, samples with a predominantly ferritic structure (P9-TFS and T22-TFS) have permeability of 83, 60.4 and 109, 72.5 for the cylindrical sensor and PCB-coil integrated sensor respectively.

Although the permeability values are not precisely the same for the three sets of measurements (cylindrical sensor, PCB-coil integrated sensor and BH curves), similar trends for the samples can be observed.

It is clear from Table 1 that coercivity has an inverse relationship with permeability (obtained from impedance measurements), as the samples with the lowest coercivity values have the highest permeability values. The coercivity values reflect the magnetic hardness of the samples, which in turn is indicative of material/physical hardness, therefore both the permeability and coercivity values are linked to magnetic and material hardness.

### 3.6. Sensitivity and error analysis

A sensitivity and error analysis on the permeability values of these power station steels obtained from the spectra, has been presented by the authors in [10,11]. However, in order to evaluate the accuracy of the  $B-H$  measurements, any change in  $B-H$  values as a result of variations in the positioning of the sample and the Hall probe has been assessed. In addition, the presence of fringing fields from the U-core and the demagnetisation fields are considered.

Initially variations in  $B-H$  values as a result of different positioning of the sample and the sensor are considered. The first test was carried out to investigate variations in  $B-H$  values due to movement of the sample with respect to the U-core, the results of which are presented in Fig. 12a. In other words, it is a way of analysing whether the position of the sample with respect to the slot in the U-core (Fig. 12b) makes any difference to the magnetic coupling between the core and the sample. As it is clear from Fig. 12a, different positions and seating of the sample on the U-core does not make a significant difference.

The purpose of the second investigation was to consider the 180° rotation of the Hall sensor (measurement setup shown in Fig. 12b), and its corresponding effect on the  $B-H$  values; results of which are shown in Fig. 12c. As it is clear from Fig. 12c, 180° rotation of the Hall sensor produces the same  $B$  values for both measurement set-ups, but higher  $H$  values for when the Hall sensor is placed on bottom of the sample; such change in  $H$  values is due to the effect of fringing fields.

The final sensitivity test was to analyse the kind of errors one can get by miss-positioning the Hall sensor on the surface of the sample. For this sensitivity analysis, a total of 21 measurements (10 on each side and 1 at the centre of the sample) were carried out for each sample – with 2 mm increments starting from the centre of the sample and moving towards each side of the sample; the results of this analysis and the measurement set-up is presented in Fig. 13a and b respectively.

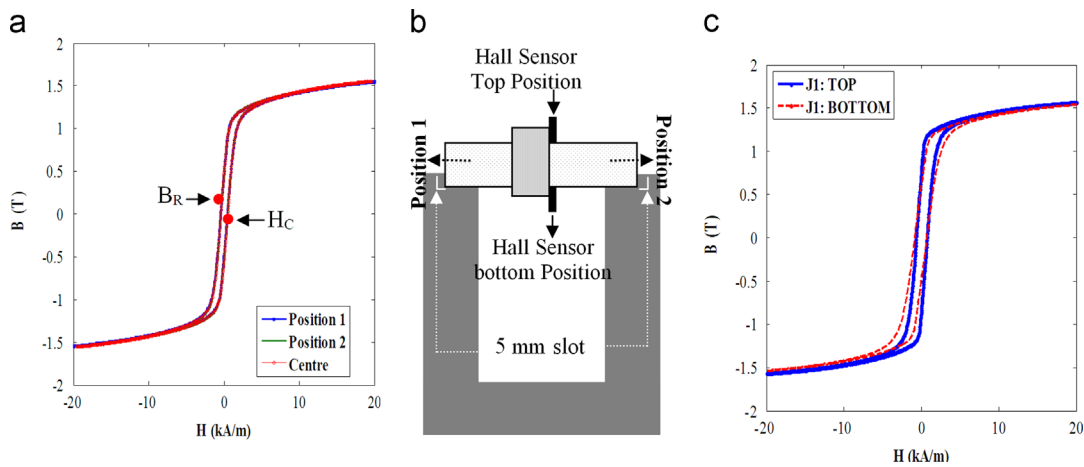


**Fig 12.** Sensitivity analysis with (a) movement of the sample with respect to the U-core, (b) sample and the sensor setup for different tests (c) 180 degree rotation of the Hall sensor.

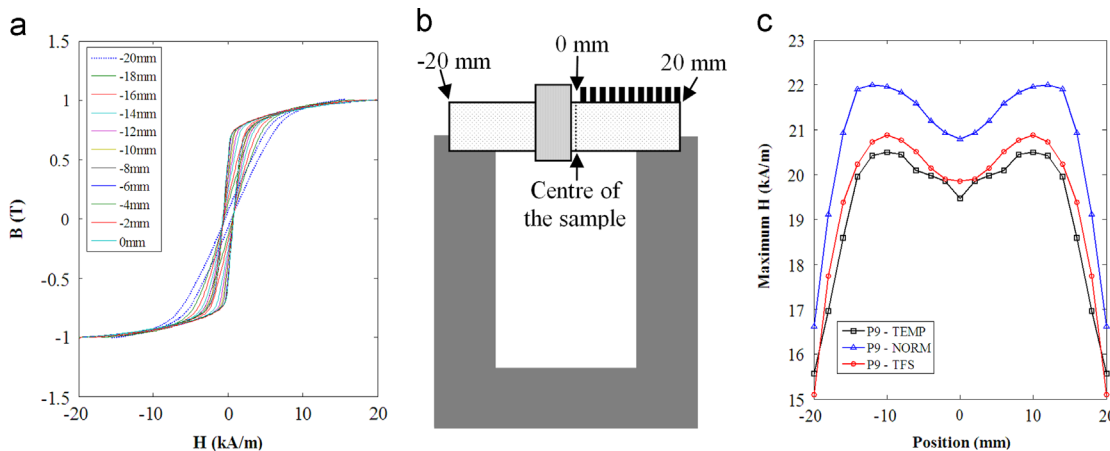


**Fig 13.** Movement of the Hall sensor on the surface of the sample (a) Hysteresis loop for P9 Tempered sample at different locations of the Hall sensor (b) the measurement set-up for the 11 tests on the surface of the sample with increments of 2 mm (c) complete measurements for the three P9 samples.

It is clear from Fig. 13a, movement of the Hall sensor on the surface of the sample does not affect the  $B$  values; this is evident by comparing the hysteresis curves for the two extreme distances (i.e. 0 mm and  $\pm 20$  mm). Such movement, however, produces a maxima in the  $H$  value at around  $\pm 12$  mm, due to the addition of the fringing field to the applied field; changes in the  $H$  values are due to the net effect on the axial component of the field of different fields such as external, demagnetisation and fringing fields. As shown in the results, positioning of the Hall sensor has considerable effect on the results and therefore this sensitivity test highlights the importance of consistent Hall sensor positioning for accurate measurements.

#### 4. Conclusions

In this paper, cylindrical air-cored and PCB-coil integrated sensors were designed to measure the EM properties of 50 mm long, 4.95 mm diameter power generation steel (P9 and T22) samples taken from ex-service pipes and tubes and also after different heat treatments. The EM properties of these steel samples, obtained through impedance measurements using the two sensor geometries were compared and analysed. Analytical and numerical methods (finite elements) were used to calculate

the sensor response, and as a result the conductivity and permeability of these samples were inferred.

The magnetic hysteresis curves for the power station steel samples were also measured, from which relative incremental permeability values were obtained. The incremental permeability values measured through minor loop deviations from the initial magnetisation curve were connected to the permeability values obtained from the spectroscopy of these samples, and their corresponding EM properties have been identified with strong correlations with material properties such as hardness. Correlations between EM properties and changes in the microstructure (normalised only, normalised and tempered and ex-service) were established, which may allow one to quantify the condition of power station steels in-situ. This could be used in future to develop a tool for in-situ inspection and could, therefore, lead to considerable savings while allowing frequent and detailed component inspection.

Based on the tools and techniques developed, and results presented in this paper, a non-destructive testing technique could be developed which could potentially be used for the assessment of thermal aging and eventual creep damage in power station tubes and pipes. Two approaches are available; the first of these is the utilisation of an encircling coil, measuring the flux density across the entire cross-section of the component, used in conjunction with a magnetising yoke. This approach has the advantage that it would

allow low frequency, high penetration depth measurements to be employed, which may be necessary where the condition of the bulk of the material is likely to be different to the surface layer, i.e. decarburisation. However, this technique could only be deployed on sections of pipe and tube where the entire circumference is accessible and measures would have to be developed to compensate for the fact that excitation would be local (i.e. over only part of the pipe/tube cross-section); whereas flux density would be measured over the entire cross-section.

Incremental permeability could also be measured by eddy current impedance measurements, where high frequency minor loops are superimposed on a  $B-H$ -loop when the eddy current frequency is a factor of 100 higher than the magnetising frequency. This technique has the advantage that only a small section of the component surface would need to be accessible, but in order to attain the required sensitivity, higher frequencies may need to be employed for the incremental permeability measurements, so penetration depth would be limited.

### Acknowledgement

The authors greatly acknowledge the financial support of The Engineering and Physical Sciences Research Council (EPSRC) for this project under contract EP/H022937.

### References

- [1] X. Ma, A.J. Peyton, Y.Y. Zhao, Eddy current measurements of electrical conductivity and magnetic permeability of porous metals, *NDT&E Int.* 39 (2006) 562–568.
- [2] R.J. Haldane, W. Yin, M. Strangwood, A.J. Peyton, C.L. Davis, Multi-frequency electromagnetic sensor measurement of ferrite/austenite phase fraction—experiment and theory, *Scr. Mater.* 54 (2006) 1761–1765.
- [3] W. Yin, A.J. Peyton, M. Strangwood, C.L. Davis, Exploring the relationship between ferrite fraction and morphology and the electromagnetic properties of steel, *Mater. Sci.* 42 (2007) 6854–6861.
- [4] X.J. Hao, W. Yin, M. Strangwood, A.J. Peyton, P.F. Morris, C.L. Davis, Off-line measurement of decarburization of steels using a multifrequency electromagnetic sensor, *Scr. Mater.* 58 (2008) 1033–1036.
- [5] M.P.H. Papaalias, M. Strangwood, A.J. Peyton, C.L. Davis, Measurement of phase transformations in steel using electromagnetic sensors, *J. Iron Making Steel Making* 29 (2002) 469–476.
- [6] G. Sposito, C. Ward, P. Cawley, P.B. Nagy, C. Scruby, A review of non-destructive techniques for the detection of creep damage in power plant steels, *NDT&E Int.* 43 (2010) 555–567.
- [7] M. Caleap, B.W. Drinkwater, P.D. Wilcox, Modelling wave propagation through creep damaged material, *NDT&E Int.* 44 (2011) 456–462.
- [8] T. Saito, H. Kitazima, Hard magnetic properties of anisotropic Sm-Fe-N magnets produced by compression shearing method, *J. Magn. Magn. Mater.* 323 (2011) 2154–2157.
- [9] A. Pulnikov, V. Permiakov, M.D. Wulf, J. Melkebeek, Measuring setup for the investigation of the influence of mechanical stresses on magnetic properties of electrical steel, *J. Magn. Magn. Mater.* 254–255 (2003) 47–49.
- [10] F. Ossart, L. Hirsinger, R. Billardon, Computation of electromagnetic losses including stress dependence of magnetic hysteresis, *J. Magn. Magn. Mater.* 196–197 (1999) 924–926.
- [11] R. Gou, Y. Zhang, X. Xu, L. Sun, Y. Yang, Residual stress measurement of new and in-service X70 pipelines by X-ray diffraction method, *NDT&E Int.* 44 (2011) 387–393.
- [12] S. Kahrobaee, M. Kashefi, Hardness profile plotting using multi-frequency multi-output electromagnetic sensor, *NDT&E Int.* 44 (2011) 335–338.
- [13] J.W. Wilson, G.Y. Tian, V. Moorthy, B.A. Shaw, *IEEE Trans. Magn.* 45 (2009) 177–183.
- [14] C. Zhang, N. Bowler, C. Lo, Magnetic characterization of surface-hardened steel, *J. Magn. Magn. Mater.* 321 (2009) 3878–3887.
- [15] S. Kobayashi, H. Takahashi, Y. Kamada, Evaluation of case depth in induction-hardened steels: Magnetic hysteresis measurements and hardness-depth profiling by differential permeability analysis, *J. Magn. Magn. Mater.* 343 (2013) 112–118.
- [16] A.T. Wilder, Power frequency magnetic properties and aging of 4130 steel, *J. Magn. Magn. Mater.* 300 (2006) L257–L261.
- [17] P. Ennis, A. Czyska-Filemonowicz, Recent advances in creep resistant steels for power plant applications, *Sadhana Acad. Proc. Eng. Sci.* 28 (2003) 709–730.
- [18] W. Yin, N. Karimian, J. Liu, X.J. Hao, L. Zhou, A.J. Peyton, M. Strangwood, C.L. Davis, Measurement of electromagnetic properties of power station steels, *I2MTC IEEE Int.* (2012) 1603–1606.
- [19] W. Yin, N. Karimian, J. Liu, X.J. Hao, L. Zhou, A.J. Peyton, M. Strangwood, C.L. Davis, Measurement of electromagnetic properties of power station steels, *NDT&E Int.* 51 (2012) 135–141.
- [20] T. Slawomir, Induction coil sensors, *Meas. Sci. Technol.* 18 (2007) R31–R46.
- [21] H. Griffiths, Magnetic induction tomography, *Meas. Sci. Technol.* 12 (2001) 1126–1131.
- [22] A.J. Peyton, Z.Z. Yu, G.M. Lyon, An overview of electromagnetic induction tomography: description of three different systems, *Meas. Sci. Technol.* 7 (1996) 261–271.
- [23] H.Y. Wei, M. Soleimani, Three-dimensional magnetic induction tomography imaging using a matrix free Krylov subspace inversion algorithm, *Prog. Electromagn. Res.* 122 (2012) 29–45.
- [24] L. Ma, H.Y. Wei, M. Soleimani, Pipelines in section using magnetic induction tomography based on a narrowband pass filtering method, *Prog. Electromagn. Res.* 23 (2012) 65–78.
- [25] W. Yin, A.J. Peyton, Sensitivity formulation including velocity effects for electromagnetic induction systems, *IEEE Trans. Magn.* 46 (2010) 1172–1176.
- [26] M.H. Pham, A.J. Peyton, A model for the forward problem in magnetic induction tomography using boundary integral equations, *IEEE Trans. Magn.* 44 (2008) 2262–2267.
- [27] W. Yin, A.J. Peyton, A planar EMT system for the detection of faults on thin metallic plates, *Meas. Sci. Technol.* 17 (2006) 2130–2135.
- [28] C. Akyel, S.I. Babic, M.M. Mahmoudi, Mutual inductance calculation for non-coaxial circular air coils with parallel axes, *Prog. Electromagn. Res.* 91 (2009) 287–301.
- [29] O. Biro, Edge element formulations of eddy current problems, *Comput. Methods Appl. Mech. Eng.* 169 (1999) 391–405.
- [30] P. Zhao, H.G. Wang, Resistances and inductances extraction using surface integral equation with the acceleration of multilevel Green function interpolation method, *Prog. Electromagn. Res.* 83 (2008) 43–54.
- [31] H.G. Wang, P. Zhao, Combining multilevel Green's Function interpolation method with volume loop bases for inductance extraction problems, *Prog. Electromagn. Res.* 80 (2008) 225–239.
- [32] R. Ravaut, G. Lemarquand, V. Lemarquand, S.I. Babic, C. Akyel, Mutual inductance and force exerted between thick coils, *Prog. Electromagn. Res.* 102 (2010) 367–380.
- [33] J. Liu, X.J. Hao, L. Zhou, M. Strangwood, C.L. Davis, A.J. Peyton, *Scr. Mater.* 66 (2012) 367–370.
- [34] P. Novotny, P. Machac, P. Sajdl, Diagnostics of austenitic steels by coercivity mapping, *NDT&E Int.* 41 (2008) 530–533.
- [35] I.D. Mayergoyz, *Mathematical Models of Hysteresis*, Springer, New York, 1991.
- [36] G. Bertotti, *Hysteresis in Magnetism*, Academic Press, USA, 1998.
- [37] E. Della Torre, *Magnetic Hysteresis*, IEEE Press, Piscataway, NJ, 2000.
- [38] M. Carpentieri, G. Finocchio, F.L. Foresta, B. Azzerboni, State-independent hypothesis to model the behavior of magnetic materials, *J. Magn. Magn. Mater.* 280 (2004) 158–163.
- [39] G. Bertotti, *Hysteresis in Magnetism: for Physicists, Materials Scientists, and Engineers*, Academic Press, San Diego, 1998.